nature electronics

Article

https://doi.org/10.1038/s41928-023-01056-1

Programmable graded doping for reconfigurable molybdenum ditelluride devices

Received: 21 October 2022

Accepted: 3 October 2023

Published online: 13 November 2023

Check for updates

Ruixuan Peng[1], Yonghuang Wu[1], Bolun Wang[1], Run Shi[1], Longlong Xu[1], Ting Pan[1,2], Jing Guo[1], Bochen Zhao[1], Cheng Song[1], Zhiyong Fan[3], Chen Wang[1], Peng Zhou[4], Shoushan Fan[2] & Kai Liu[1] ✉

Non-volatile reconfigurable devices have the potential to improve integration levels and lower power consumption in next-generation electronics. Two-dimensional semiconductors are promising materials for making non-volatile reconfigurable devices due to their atomic thinness and strong gate control, but it is challenging to create varied reconfigurable functions with a simple device configuration. Here we show that an effective-gate-voltage-programmed graded-doping strategy can be used to create a single-gate two-dimensional molybdenum ditelluride device with multiple reconfigurable functions. The device can be programmed to function as a polarity-switchable diode, memory, in-memory Boolean logic gates and artificial synapses with homosynaptic plasticity and heterosynaptic plasticity. As a diode, the device exhibits a rectification ratio of up to 10^4; as an artificial heterosynapse, it shows heterosynaptic metaplasticity with a modulatory power consumption that can be reduced to 7.3 fW.

Large-scale next-generation electronics will require field-effect transistors (FETs) that are highly miniaturized and have multiple functionalities. However, short-channel effects limit the downscaling of traditional FETs to sub-10 nm feature sizes and hinder the extension of device functions[1]. Reconfigurable devices, which can switch their functions during operation for different tasks, have been proposed as an alternative. However, reconfigurable devices based on silicon FETs need to combine complex electronic circuits and additional memory units to perform and store the reconfiguration, which increases system complexity, reduces the integration level and complicates the fabrication process[2]. It is, therefore, desirable to develop advanced reconfigurable devices with simple configurations and using non-silicon materials[3,4]. Two-dimensional (2D) semiconductors, such as transition metal dichalcogenides, have been explored for use in reconfigurable electronic devices. Due to their layered, dangling-bond-free structures, 2D semiconductors have unique electronic properties[1] and can offer a wide range of configurations and functions[5–12].

Controllable and reversible doping is the key to develop reconfigurable 2D devices. Since traditional ion implantation doping methods used in silicon-based devices are not suitable for 2D semiconductors due to their atomic thickness[1], doping strategies including the adsorption/desorption of molecules[13,14], charge trapping[15] and ferroelectric polarization[16] have been employed to create reconfigurable 2D devices. Electrostatic gating can be used to control the doping level of these devices. However, single-gate reconfigurable devices are mostly limited to dual or triple functions, for example, n- and p-type FETs and/

[1]State Key Laboratory of New Ceramics and Fine Processing, School of Materials Science and Engineering, Tsinghua University, Beijing, China. [2]State Key Laboratory of Low-Dimensional Quantum Physics, Department of Physics and Tsinghua-Foxconn Nanotechnology Research Center, Tsinghua University, Beijing, China. [3]Department of Electronic and Computer Engineering, The Hong Kong University of Science and Technology, Clear Water Bay, Kowloon, Hong Kong SAR, China. [4]State Key Laboratory of ASIC and System, School of Microelectronics, Fudan University, Shanghai, China. ✉e-mail: liuk@tsinghua.edu.cn

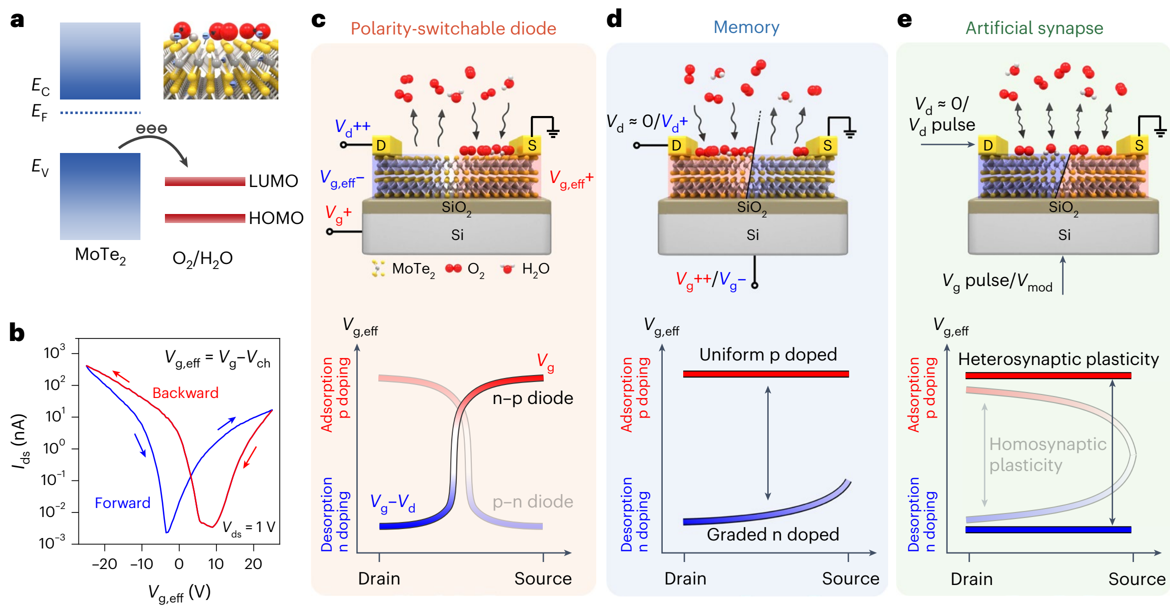

Fig. 1 | Schematic and working principle of a single-gate reconfigurable $MoTe_2$ device. a, Schematic of the charge transfer process between the $MoTe_2$ channel and adsorbed O_2/H_2O molecules. The inset shows a schematic of the electron transfer process from $MoTe_2$ to O_2/H_2O molecules. HOMO, highest occupied molecular orbital; LUMO, lowest unoccupied molecular orbital; E_F, Fermi level; E_C, conduction band edge; E_V, valence band edge. **b**, Transfer characteristics of the $MoTe_2$ device at $V_{ds} = 1$ V. The effective gate voltage $V_{g,eff}$ equals the applied gate voltage because V_d and V_s are small. **c**, Schematic of the $MoTe_2$ device under the configuration process to an n–p diode (top). The distribution of $V_{g,eff}$ is superimposed for clarity. Line profile of $V_{g,eff}$ distribution under the configuration process to n–p diode or p–n diode (bottom). **d**, Schematic of the reconfigurable device as a memory (top). The configuration process to the uniform p-doped state and graded n-doped state is illustrated on the left and right, respectively. Corresponding line profile of $V_{g,eff}$ distribution (bottom). **e**, Schematic of the device as an artificial heterosynapse. Here, V_g or V_d pulses, either positive or negative, are applied to modulate the synaptic weight. $V_{g,eff}$ distribution under either V_g stimuli (for the emulation of the homoeostatic function of heterosynaptic plasticity) or V_d stimuli (for the emulation of homosynaptic plasticity) (bottom).

or homosynaptic transistors. To achieve more reconfigurable functions, multiple gates are fabricated to control doping separately and locally, though this increases system complexity and manufacturing cost[3,9,17–19]. Other structures for reconfigurable 2D devices have also been reported, such as semi-floating gate[20], half-charge-tunnelling layer[7], half-ferroelectric layer[21], ionic conductive layer[22] and heterojunctions[23,24], but the problem of high system complexity remains.

In this Article, we report an effective-gate-voltage-programmed graded-doping (EGV-pGD) strategy and use it to reconfigure a single-gate ambipolar molybdenum ditelluride ($MoTe_2$) device to multiple states. By simultaneously applying a large drain–source voltage and a gate voltage, a graded effective gate voltage is induced across the $MoTe_2$ device, which precisely controls the adsorption and desorption of gas molecules on the channel. The reconfigurable device can function as polarity-switchable diodes, memory, in-memory Boolean logic and artificial synapses with homosynaptic plasticity and heterosynaptic plasticity (Supplementary Table 1 lists a comparison with other reconfigurable 2D devices). The reconfigurable functions of the device also show high performance. In particular, as a diode, the device exhibits a rectification ratio up to 10^4, and as an artificial heterosynapse, the device shows heterosynaptic metaplasticity with a modulatory power consumption under 10 fW. Our work provides a simple EGV-pGD strategy to realize reconfigurable multifunctionality in 2D devices with low complexity of device configuration and improves the understanding of gate-controlled doping for 2D ambipolar semiconductors.

Working principle of reconfigurable $MoTe_2$ devices

Figure 1 illustrates the working principle of the reconfigurable $MoTe_2$ device with switchable functions among p–n/n–p diodes, memory and homosynaptic/heterosynaptic plasticity. A variety of switchable functions are enabled in a single-gate device by reconfigurable EGV-pGD due to the programmable adsorption/desorption of molecules on $MoTe_2$. Supplementary Fig. 1 shows the atomic force microscopy image and Raman spectra of a typical device. $MoTe_2$ is a 2D ambipolar semiconductor with a bandgap of 0.9 to 1.1 eV, depending on its thickness[25]. The ambipolarity of the $MoTe_2$ channel is vital for reconfigurability because it allows $MoTe_2$ to be n doped, p doped or graded doped, as desired. Moreover, the near-zero threshold voltage (V_{th}) of the ambipolar $MoTe_2$ is also important for high-performance reconfigurable functions (Supplementary Note 1 provides a detailed discussion). It is known that the lowest unoccupied molecular orbit of O_2 and H_2O molecules is lower than the valence band maximum of $MoTe_2$, which leads to electron transfer from the $MoTe_2$ channel to the adsorbates and thus p-type doping of the channel (Fig. 1a)[26,27]. The large clockwise hysteresis in the transfer curve measured in air (Fig. 1b and Supplementary Fig. 2a) versus the negligible hysteresis measured in a vacuum (Supplementary Fig. 2b,c) confirms the adsorption/desorption of molecules. When a positive V_g is applied, the electron density in the channel rises, which facilitates the adsorption of O_2/H_2O molecules. The adsorbates remain on the channel after V_g is removed, and as a result, the channel is p doped, and the transfer curve is positively shifted. In contrast, a negative V_g depletes the electrons of the channel, which leads to weakened adhesion between the channel and the adsorbates and promotes the desorption of adsorbates. This results in a negative shift in the transfer curve and n doping of the channel compared with that before applying the negative V_g (refs. 13,28,29).

In real cases, the EGV (also represented by $V_{g,eff}$), defined as the relative voltage between the channel and gate terminal, is more critical than V_g to determine the doping states of $MoTe_2$, which follows the relationship

https://doi.org/10.1038/s41928-023-01056-1

$$V_{g,\mathrm{eff}}(x) = V_g - V_{\mathrm{ch}}(x), \quad (1)$$

where V_g is the global gate voltage and $V_{ch}(x)$ is the local electrical potential of a channel. Therefore, $V_{g,eff}(x)$ determines the real gate voltage distribution along the channel. When the absolute values of the source and drain voltages (V_s and V_d, respectively) are much smaller than that of V_g, $V_{g,eff}$ nearly equals V_g as V_{ch} is negligible, which is the common case for an FET. However, if the drain–source voltage (V_{ds}) is large enough compared with a large V_g in absolute values, $V_{g,eff}$ will be highly non-uniform along the channel[30]. Such a large V_{ds} is known to induce a pinch-off effect in traditional Si-based FETs[31]. In 2D FETs, graded doping of the channel will occur due to the non-uniform adsorption/desorption of O_2/H_2O molecules. As $MoTe_2$ is ambipolar and its polarity is very sensitive to the doping level, this single-gate $MoTe_2$ device can be configured towards multiple states by simultaneously applying different sets of gate and drain voltages in air.

Specifically, to construct an n–p diode, a positive V_d is set to be larger than a positive V_g, and the source terminal is grounded (Fig. 1c, top), such that V_{ds} is large to induce a large variation in $V_{ch}(x)$. Consequently, in the region near the drain electrode, $V_{g,eff}$ (drain) = $V_g - V_d$ is negative since V_d is higher than V_g, which promotes O_2/H_2O desorption and leads to n doping. Near the source electrode, in contrast, $V_{g,eff}$ (source) = $V_g > 0$, leading to the adsorption of molecules and p doping. As a result, an n–p diode is formed. Similarly, a p–n junction can be made by applying large negative V_d and V_g.

To realize and enhance the memory function of the reconfigurable device, a p-doped state of $MoTe_2$ is formed by applying a large positive V_g with a small V_d, which has $V_{g,eff}$ uniform and positive leading to uniform p doping over the channel. For the n-doped state, negative V_g and positive V_d are simultaneously applied to induce graded n doping over the channel. As $V_{g,eff}$ is lower, the n-doping level is deeper near the drain than near the source, which greatly enhances the retention performance of the memory (Fig. 1d).

Moreover, the reconfigurable $MoTe_2$ device can also emulate a biological heterosynapse with functions of both homosynaptic and heterosynaptic plasticity (Fig. 1e). The drain and source terminals are defined as pre- and postsynapse, respectively, and the channel current is defined as the synaptic weight between them. The gate terminal represents a modulatory synapse. The synaptic weight can be adjusted by the stimuli of positive or negative V_g pulses as an emulation of the homoeostatic function of heterosynaptic plasticity. The weight can also be altered by V_d pulses, which changes the $V_{g,eff}$ distribution over the channel and promotes gas adsorption/desorption. This homosynaptic plasticity can be modulated by the gate terminal (V_{mod}), representing heterosynaptic metaplasticity.

EGV-pGD for polarity-switchable diodes

It is well known that p–n junctions are key components in modern electronic and optoelectronic devices[17,31]. Typically, complex device structures and complicated fabrication processes are essential for non-volatile polarity-switchable diodes[17,22]. In sharp contrast, our reconfigurable $MoTe_2$ device can work as non-volatile polarity-switchable diodes with only one gate terminal required. As shown in Fig. 2a, when V_g is set to 19 V, V_d to 28 V and the source grounded, $V_{g,eff}$ varies from −9 to 19 V from the drain to source. This leads to the graded doping of the $MoTe_2$ channel, ranging from n doping around the drain to p doping around the source, due to the desorption and adsorption of O_2/H_2O, respectively. As a result, an n–p diode forms along the channel. Similarly, a p–n diode can be configured or reconfigured on the same device when $V_g = -9$ V and $V_d = -28$ V. It is worth noting that an abrupt $V_{g,eff}$ transition exists between the n-doped and p-doped regions due to the pinch-off effect (Fig. 2b). This indicates that the undoped region (where $V_{g,eff}$ is close to zero) is narrow, leading to a relatively sharp n–p or p–n junction in the middle of the channel (Supplementary Notes 2 and 3 provide a detailed derivation)[32,33]. The position of this sharp transition can be well controlled by the sets of V_d and V_g (Fig. 2c and Supplementary Figs. 3 and 4). Specifically, the transition region moves from the drain to the source electrode with decreasing V_g or increasing V_d. We used Kelvin probe force microscopy (KPFM) to verify the doping states of the channel. As shown in Fig. 2d, in the regions where positive $V_{g,eff}$ values are applied, the surface potential of the channel is lower because of the transfer of electrons from the channel to the adsorbates, verifying the p doping of the channel. In contrast, the surface potential is higher in the regions where negative $V_{g,eff}$ values are applied because of the n-doping effect due to the desorption of most adsorbates. In both n–p and p–n diodes, clear boundaries exist between the n-doped and p-doped regions. The line profiles of the surface potential along the channel suggest that the boundaries are relatively sharp (Fig. 2e), which validates the formation of relatively sharp junctions. The depletion region is further determined to be narrower than 400 nm, as shown by the optimized KPFM measurements and the short-channel device (Supplementary Note 4).

Both output characteristic curves of the n–p and p–n diodes reveal typical current-rectifying behaviours, with rectification ratios of ~1.4×10^4 and ~1.1×10^3, respectively (Fig. 2f). These output curves can be fitted to the Shockley diode equation, $I = I_0[\exp\left(\frac{qV_D}{nkT}\right) - 1]$, where I_0 is the reverse saturation current; n is the ideality factor; and k, T and q are the Boltzmann constant, temperature and elementary charge, respectively[31]. The ideality factors of the n–p and p–n states are 1.93 and 1.84, respectively, both close to 2.00. This indicates that the recombination current—rather than the diffusion current—is dominant in the carrier transport process, possibly resulting from a large density of trap states introduced by the adsorbates[17,31]. The slight difference in the rectification ratio mainly results from the different position of the junction region and the non-uniformity of the $MoTe_2$ channel (Supplementary Note 5). In addition to the switchable polarity, the $MoTe_2$ diode also shows an obvious photoresponse (Fig. 2g and Supplementary Fig. 5), which originates from the separation of photogenerated electrons and holes owing to the large built-in potential in the junctions. Under positive (negative) V_{ds}, the built-in potential of the n–p (p–n) diode is enhanced, and thus, a substantial photocurrent is observable. The short-circuit photocurrent of the n–p (p–n) diode increases (decreases) with increasing incident light power (Supplementary Fig. 6). For comparison, the same device under a uniformly n-doped or p-doped state shows a negligible photoresponse compared with the device in an n–p or p–n diode state, verifying that the photoresponse of the diode arises from the junction area instead of the p-doped or n-doped region (Supplementary Fig. 7).

EGV-pGD for $MoTe_2$ memory

The configuring procedure of a $MoTe_2$ memory is shown in Fig. 3a,b. In general, the p-doped state is realized by applying a large V_g (28 V) for 2 min together with negligible V_d and V_s (Fig. 3a). In this case, $V_{g,eff}$ is uniform and positive along the channel, leading to uniform p doping. For the n-doped state, $V_g = -13$ V, $V_d = 17$ V and $V_s = 0$ V are simultaneously applied (Fig. 3b). At such a high drain–source voltage, $V_{g,eff}$ gradually increases from −30 V at the drain to −13 V at the source, leading to graded n doping of the channel with a deeper doping level near the drain (Fig. 3c). Therefore, there is a large memory window of ~25 V between the transfer curves of the uniform p-doped state and graded n-doped state (Fig. 3d). For the p-doped state, the channel is homogeneously doped and can be turned off by a global gate voltage, leading to a small difference between the electron threshold voltage ($V_{th,e}$) and hole threshold voltage ($V_{th,p}$). For the n-doped state, however, the doping is heterogeneous, and the local V_{th} varies at different locations. As a result, the channel can be partially turned off by a wide range of V_g, and the transfer curve exhibits a wide switching-off region, which is beneficial for the retention and duration performance of the memory. KPFM measurements clearly reveal that the p-doped device has a much lower surface potential than the n-doped device (Fig. 3e). The difference

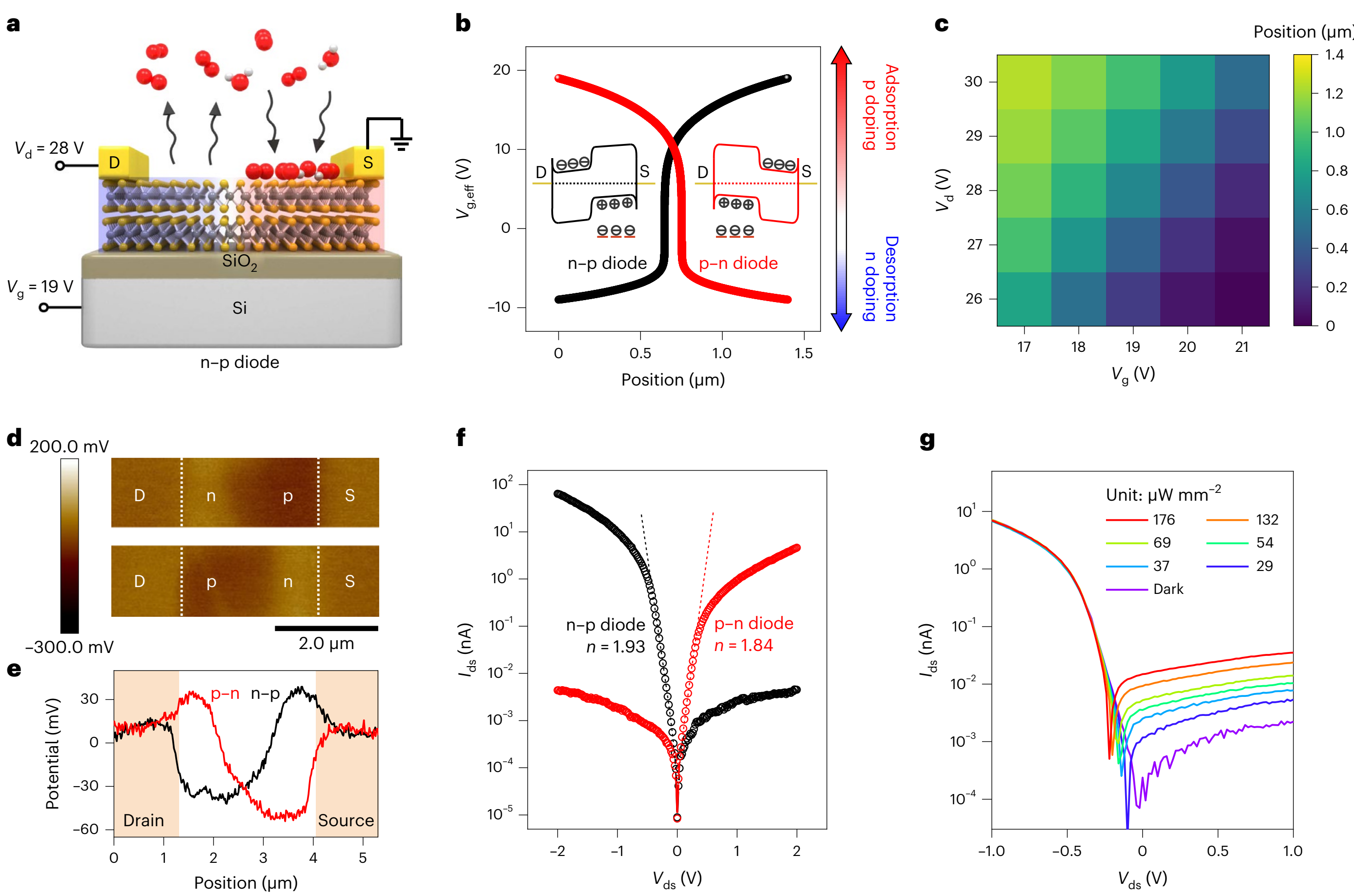

Fig. 2 | Polarity-switchable $MoTe_2$ diodes based on EGV-pGD. a, Schematic of a reconfigurable $MoTe_2$ device under configuration to an n–p diode. **b**, Distribution of $V_{g,eff}$ under configuration to n–p diode and p–n diode. The inset shows the corresponding band diagram after the configuration process. **c**, Dependence of the position where $V_{g,eff}$ = 0 V on a simultaneous change in V_g and V_d. The drain electrode locates at position x = 0 and the source at position x = 1.4 μm. **d**, KPFM images of the polarity-switchable n–p and p–n diodes. The measurements are conducted under the protection of Ar gas flow. Here 'S' and 'D' denote the source and drain electrode, respectively. **e**, Line profiles of the surface potential of the diodes. **f**, Output characteristics of the reconfigurable n–p and p–n diodes fitted to the Shockley diode equation. The open circle dots are the data points, and the dotted lines are the fitted curves. **g**, Optoelectrical characteristics of the reconfigurable n–p diode under different light power densities.

in surface potential between the p-doped and n-doped states is 113 mV (Fig. 3f). We note that the device experienced a short-term exposure to air when transferred to the KPFM equipment, where it was protected by the Ar gas flow. Thus, the n-doped device unavoidably adsorbed some O_2/H_2O molecules during the transfer, and the measured surface potential of the n-doped device should be lower than the actual value.

As shown in Fig. 3g, the $MoTe_2$ memory exhibits a long retention time of more than 36 h in a vacuum, with an on/off ratio higher than 10^3. During this long-term test in a vacuum, the channel current slightly decreases in the p-doped state, which should result from O_2/H_2O desorption, whereas it gradually increases in the n-doped state, possibly due to the readsorption of residual O_2/H_2O molecules in a vacuum (Fig. 3g and Supplementary Fig. 8). The graded n doping has greatly counteracted the readsorption and enhanced the retention performance by inducing a wide switching-off region. The graded n-doped device exhibits a switching-off region wider than 7 V, whereas that of the uniformly n-doped state is narrower than 1 V (Supplementary Fig. 9a). Since the memory device is read under a constant gate voltage, a wider switching-off region provides a better capability of the device to maintain a low read current (Supplementary Fig. 9b). As a result, the read current of the graded n-doped state remains lower than 1 pA for more than 20 h, showing much better retention performance than the uniform n-doped state (Fig. 3h). Under an endurance test with repeatedly adsorbing and desorbing gas molecules (Supplementary Fig. 10a), the memory device shows steady read currents and an on/off ratio over 10^3 after 500 cycles, exhibiting good endurance performance. The Raman spectrum after the endurance test shows no oxidation peak (Supplementary Fig. 10b), implying that O_2/H_2O molecules do not form chemical bonds with $MoTe_2$ and the adsorption process was physical adsorption (Supplementary Note 6). The transfer curve of the device exhibits a negligible shift after configuring in a vacuum and a large positive shift in atmosphere, verifying the proposed mechanism of gas adsorption/desorption (Supplementary Fig. 11).

By controlling the doping level of the channel, multilevel storage can be further realized (Fig. 3i). The $MoTe_2$ device is first set to a high-resistance state by applying a negative V_g, which leads to O_2/H_2O desorption and a negative shift in V_{th}. Then, five incremental positive V_g pulses are successively applied to induce O_2/H_2O adsorption and consequentially a positive shift in V_{th}. As a result, I_{ds} increases after each voltage pulse, and five distinct current levels can be clearly distinguished. The device is reset to the high-resistance state by another negative V_g pulse afterwards. Furthermore, the $MoTe_2$ device has the function of in-memory logic based on the correlation among V_g, V_d and V_s. When the gate terminal is grounded, either positive V_d or V_s can induce a large negative $V_{g,eff}$ on the channel and decrease the current, corresponding to NOR logic (Supplementary Fig. 12). When the source

https://doi.org/10.1038/s41928-023-01056-1

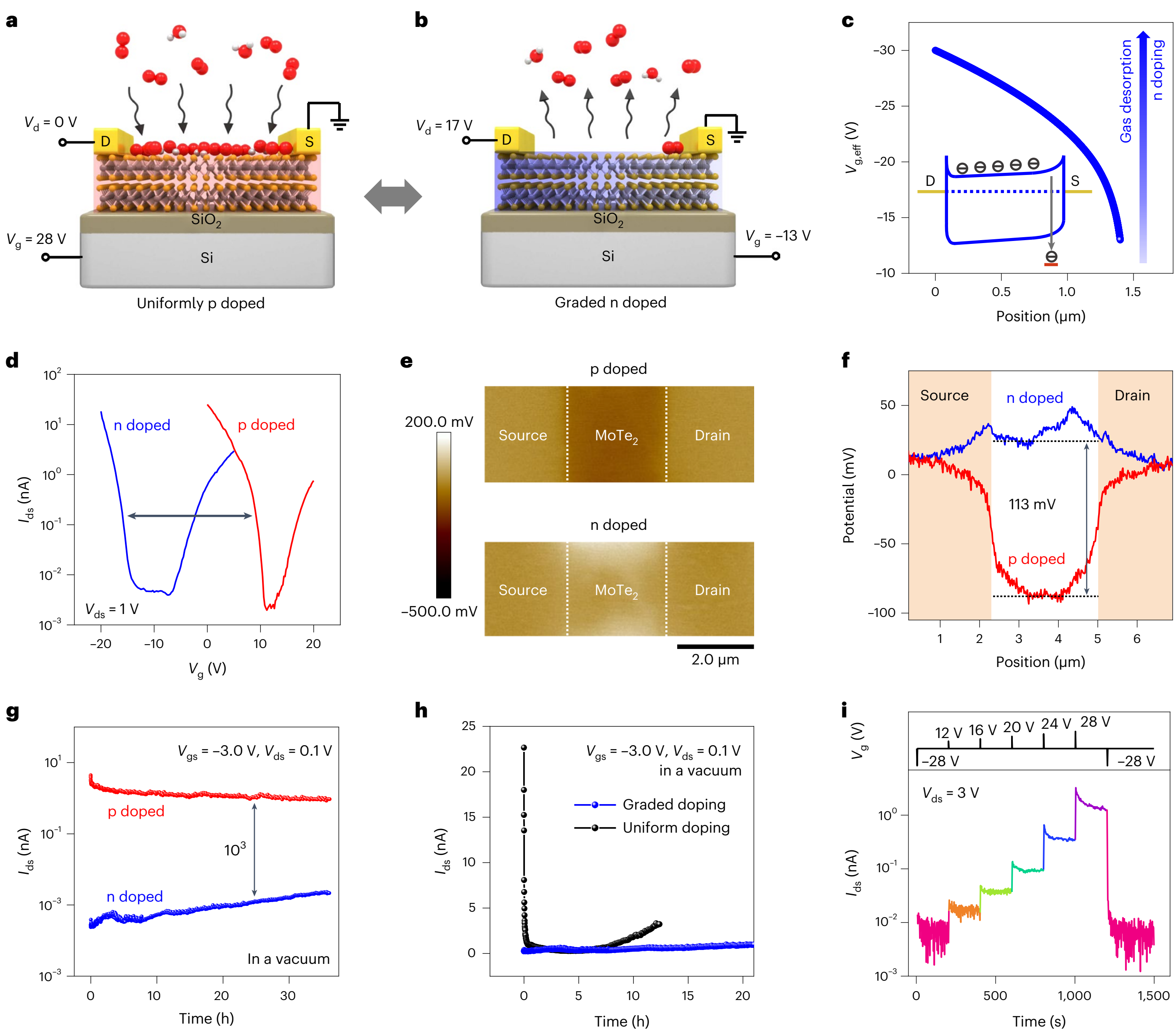

Fig. 3 | Reconfigurable $MoTe_2$ memory based on EGV-pGD. a, Schematic of a reconfigurable $MoTe_2$ memory under the configuration process to a uniformly p-doped state. **b**, Schematic of the device under the configuration process to a graded n-doped state. **c**, Distribution of $V_{g,eff}$ under the configuration process to a graded n-doped state. The speed of gas desorption is faster, and the p-doping level is deeper near the drain. The inset illustrates the band diagram of the graded n-doped device. **d**, Transfer curves of the device under graded p-doped and uniformly n-doped state. The drain–source voltage was set at 1 V. **e**, KPFM images of a device in uniform p-doped and n-doped states. The measurements are conducted under the protection of an Ar gas flow. **f**, Line profiles of the surface potential. **g**, Retention characteristics of the $MoTe_2$ memory. The current of each state was measured in a vacuum for 5 s at a time. The intervals between each measurement were 10 s at first and gradually increased to 600 s. The gate–source voltage was −3.0 V, and the drain–source voltage was 0.1 V. **h**, Retention characteristics of the device in graded n-doped and uniformly n-doped states. **i**, Evolution of the channel current after V_g pulses of different amplitudes, showing the multilevel storage ability of the device. The pulse widths are 2.0 s for negative pulses and 0.2 s for positive pulses.

terminal is grounded, a small positive V_g or small negative V_d alone cannot increase the current. However, when they are concurrently applied, large positive $V_{g,eff}$ values are induced, and the channel current rises, corresponding to AND logic (Supplementary Fig. 13).

Homosynaptic plasticity induced by EGV-pGD

The reconfigurable $MoTe_2$ device is suitable for polarity-switchable diodes and memory but is also capable of emulating a three-terminal biological heterosynapse. In biological nervous systems, the synapse is the connection between biological neurons[34,35]. Information is transmitted from one neuron to the next through synapses. A synapse that connects two information-transmitting neurons is called a homosynapse, in which the synaptic weight is the connectivity between the two neurons and synaptic plasticity describes the adjustability of the synaptic weight. Once an action potential arrives at the presynapse, neurotransmitters are released to deliver information to the postsynapse and alter the synaptic weight. This input-specific adjustment of the synaptic weight, termed homosynaptic plasticity, underlies memory and learning and can be regulated by modulatory interneurons. A synapse can also involve—in addition to information-transmitting

https://doi.org/10.1038/s41928-023-01056-1

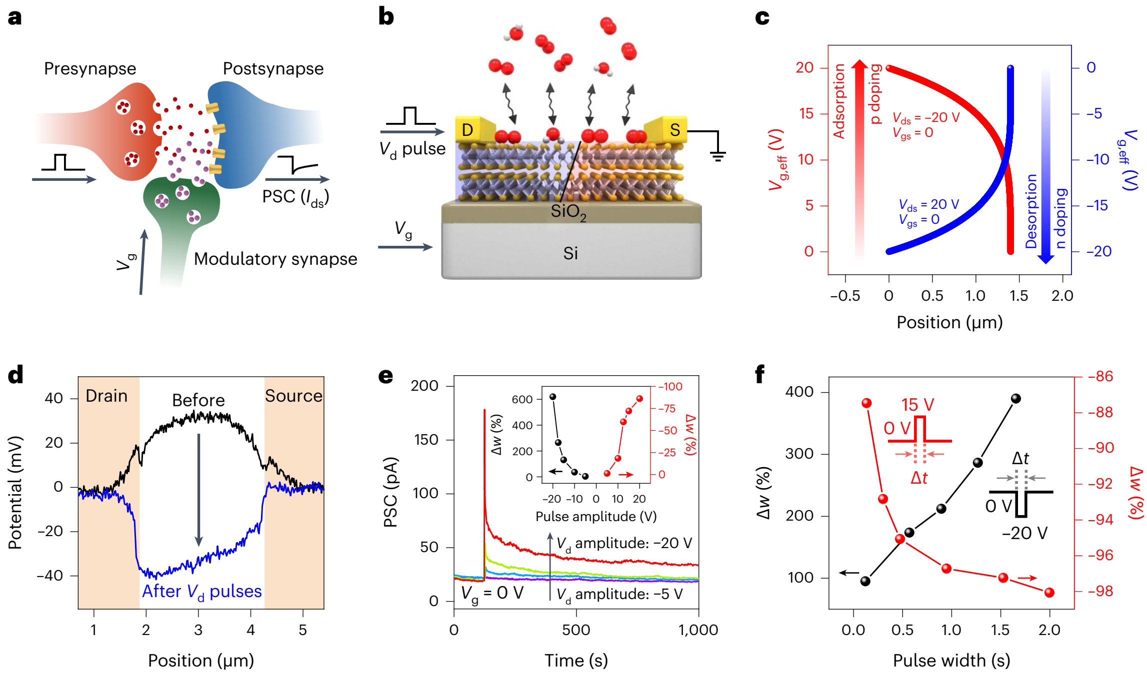

Fig. 4 | Homosynaptic plasticity in $MoTe_2$ artificial synapse. a, Schematic of a biological heterosynapse. The synaptic weight is adjusted by presynaptic stimuli. This homosynaptic plasticity can be adjusted by modulatory synapses. **b**, Schematic of a $MoTe_2$ artificial synapse. The synaptic weight (channel conductance) is adjusted by a presynaptic spike, represented by a V_d pulse. This homosynaptic plasticity is altered by modulatory neurotransmitters, represented by the V_g input. **c**, Distribution of $V_{g,eff}$ under V_d stimuli with an amplitude of ±20 V. Most of the channel is under $|V_{g,eff}|$ larger than 10 V. **d**, KPFM line profile of a $MoTe_2$ artificial synapse before and after 100 V_d pulses with an amplitude of −20 V and a width of 0.1 s. **e**, EPSC after negative V_d pulses with amplitudes from −5 to −20 V. The pulse width is 1 s. The inset shows the extracted weight change under different pulse amplitudes. **f**, Dependence of weight change on V_d pulse width. The amplitude is 15 V for positive stimuli and −20 V for negative stimuli.

neurons—modulatory neurons that are not active in information transmission. This multiterminal synapse, called a heterosynapse, has better synapse specificity and stability, as discussed later.

To emulate a biological heterosynapse, the drain and source terminals of the $MoTe_2$ device are defined as the presynapse and postsynapse, respectively, and the gate terminal is used as a modulatory synapse (Fig. 4a,b). The synaptic weight is represented by a postsynaptic current (PSC), namely, I_{ds}. To emulate homosynaptic plasticity, the stimuli of V_d pulses are applied with the source terminal grounded. The gate terminal is grounded or biased, indicating that the modulatory synapse is silent or active in the adjustment of homosynaptic plasticity, respectively. We first set V_g as 0 V to investigate the homosynaptic behaviour without heterosynaptic modulation. The distribution of $V_{g,eff}$ under negative and positive V_d pulses is illustrated in Fig. 4c. Under a V_d pulse of −20 V, $V_{g,eff}$ near the drain is 20 V as the gate terminal is grounded, inducing p doping over there, whereas $V_{g,eff}$ near the source remains 0 V. Since V_{th} is near 0 V, the channel is pinched off near the source, and thus, $V_{g,eff}$ changes more rapidly there. As a result, most of the channel is graded p doped under a large positive $V_{g,eff}$, leading to a deeper doping level near the drain and a large increase in the PSC. Under positive V_d pulses, the mechanism is similar, which results in a large negative $V_{g,eff}$ over most of the channel and reduces the PSC. KPFM measurements reveal that the surface potential of the channel is uniform before V_d pulses but decreases and becomes lower near the drain than the source after the pulses (Fig. 4d and Supplementary Fig. 14), indicating a deeper p-doping level near the drain, which is consistent with the calculated $V_{g,eff}$ distribution in Fig. 4c. This further verifies the proposed mechanism of homosynaptic plasticity.

Excitatory postsynaptic currents (EPSCs) after negative V_d pulses with different amplitudes are shown in Fig. 4e. EPSCs rapidly decay in the first 100 s after the stimuli, probably due to the desorption of weakly attached adsorbates or the release of trapped charges, followed by a slow decline afterwards. However, EPSCs become stable for 1,000 s, indicating a long-term modification of the synaptic weight. This long-term plasticity is consistent with the good retention performance of $MoTe_2$ memory. Furthermore, inhibitory postsynaptic currents after positive V_d pulses are measured (Supplementary Fig. 15), and the dependence of weight changes (Δw) on the amplitude and sign of V_d pulses is extracted (Fig. 4e, inset). The absolute value of Δw rises with increasing V_d amplitude. Homosynaptic weight change is also affected by the width of the V_d pulses (Fig. 4f and Supplementary Fig. 16). The absolute value of weight change is larger for wider V_d pulses because gas molecules are adsorbed/desorbed more completely. Meanwhile, the weight change in a vacuum is negligible compared with that in air, proving that the homosynaptic plasticity results from gas adsorption/desorption (Supplementary Fig. 17). To further validate the mechanism, EPSCs after negative V_d pulses are measured with the gate terminal either floated or grounded (Supplementary Fig. 18). EPSCs reach 3,500 pA and show long-term facilitation when the gate is grounded, whereas only small short-term facilitation is observed when the gate is floated (Supplementary Note 7). This comparison rules out the direct influence of the lateral electric field V_{ds} on homosynaptic plasticity, since the status of the gate terminal is irrelevant to V_{ds}. Moreover, it indicates that EGV-pGD cannot be fully exterminated by setting the gate terminal either grounded or floated, which should be carefully considered for other 2D FETs if large drain–source voltages are applied. We also note that the relatively large V_d used for reconfiguring diverse functions does not affect the reconfiguration and stability of our $MoTe_2$ device, because the largest electric field applied on the device is much lower than the breakdown electric field and the temperature rise induced by the large V_d is negligible (Supplementary Note 8).

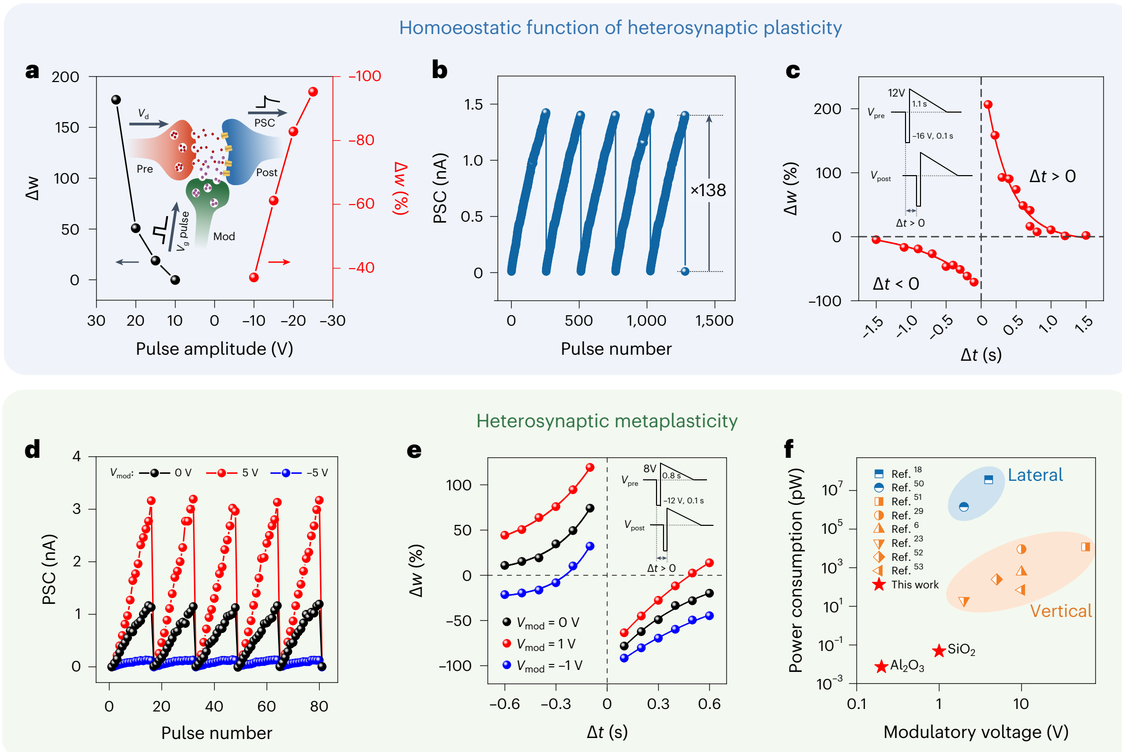

Fig. 5 | Heterosynaptic plasticity in $MoTe_2$ artificial synapse. Heterosynaptic characteristics of the $MoTe_2$ artificial synapse. **a**, Dependence of weight change (Δw) on V_g pulse amplitude. The pulse width is 2.6 s. The inset illustrates a biological heterosynapse under the homoeostatic modulation of heterosynaptic plasticity. The synaptic weight is modulated by input V_g pulses. **b**, Five consecutive cycles of LTP and LTD measurements with 256 resistance states. The amplitude and width of positive V_g pulses are 18 V and 0.1 s, and the amplitude and width of negative V_g pulses are −28 V and 5.0 s. **c**, Heterosynaptic STDP characteristics of the device. The balls are the experimental data, and the solid lines are the fitted curves. The inset shows the shape of the input spike and the definition of the time interval. **d**, LTP and LTD performance with the drain terminal as the input and the gate terminal as the modulatory terminal. The amplitude and width of the V_d pulses are −15 V and 0.1 s, respectively, for positive pulses and 15 V and 1.0 s, respectively, for negative pulses. V_g pulses (if any) are simultaneously applied with V_d pulses. **e**, Homosynaptic STDP modulated by the gate terminal. The balls and solid lines are the experimental data and fitted curves, respectively. The inset shows the shape of the input spike and the definition of the time interval. V_g pulses (if any) are simultaneously applied with V_d and V_s pulses. **f**, Comparison of heterosynaptic-metaplasticity power consumption of 2D artificial heterosynapses, including devices with lateral modulatory terminals[18,50], with vertical modulatory terminals[6,23,29,51–53] and the reconfigurable $MoTe_2$ devices reported here (90-nm-thick SiO_2 and 35-nm-thick Al_2O_3 as the gate dielectric). Power consumption is calculated by multiplying the lowest modulatory voltage by the corresponding modulatory current.

Heterosynaptic plasticity induced by EGV-pGD

In addition to homosynaptic plasticity, the reconfigurable $MoTe_2$ artificial synapse can also emulate heterosynaptic plasticity, which is a vital complement to homosynaptic plasticity in real nervous systems. In biological heterosynaptic plasticity, neuromodulators are released by modulatory interneurons into the synaptic cleft between the presynapse and postsynapse to implement two functions. First, the heterosynapse can adjust the synaptic weight between the presynapse and postsynapse[36,37]. Such a homoeostatic function of heterosynaptic plasticity is responsible for stabilizing the neural system and facilitating synaptic competition. Second, it can modulate the homosynaptic plasticity between the presynapse and postsynapse[38,39]. Such modulation, termed as heterosynaptic metaplasticity, is vital for long-term memory and synapse specificity. Since homosynaptic plasticity and both functions of heterosynaptic plasticity correlate with each other and are crucial for biological neural systems, it is valuable for neuromorphic devices to emulate all of them[6,35,38,39]. However, although homosynaptic and heterosynaptic plasticity have been concurrently realized on 2D devices[6,11,18,29,40–42], few of them have emulated both heterosynaptic metaplasticity and the homoeostatic function of heterosynaptic plasticity at the expense of structural simplicity[18,40,42]. Our simple-structured reconfigurable $MoTe_2$ device can mimic all plasticity discussed above due to the high flexibility of the EGV-pGD mechanism.

The homoeostatic function of heterosynaptic plasticity is artificially realized by using V_g pulses as stimuli. The source terminal is grounded during the measurement, whereas a small-bias V_{ds} (typically 1 V) is applied to record the PSC. As shown in Fig. 5a, the change in synaptic weight (Δw) depends on the sign and amplitude of V_g stimuli. Positive V_g pulses increase the synaptic weight by facilitating gas adsorption, whereas negative V_g pulses lead to a decrease in synaptic weight. Under a positive V_g pulse of 25 V, Δw reaches a value of 17,700%. Both EPSCs and inhibitory postsynaptic currents are stable for 1,000 s, indicating long-term plasticity (Supplementary Fig. 19). Wider V_g pulses result in greater weight changes due to more complete gas adsorption/desorption (Supplementary Fig. 20). In addition, the synaptic weight change increases with the number of V_g pulses in air, whereas no weight change is observed in a vacuum, confirming the mechanism of gas adsorption/desorption (Supplementary Fig. 21). This $MoTe_2$ artificial synapse can emulate the behaviour of long-term potentiation (LTP) and long-term depression (LTD) with high dynamic range and linearity. As shown in Fig. 5b, the PSC is increased from 10 pA to 1.4 nA under 255 positive V_g pulses and is refreshed to 10 pA by one negative V_g pulse. This unidirectional modification of synaptic weight is suitable for hardware neural networks that feature a unidirectional weight-updating method[43,44]. Our device exhibits a dynamic range of 138, low nonlinearity value of 0.56 and low cycle-to-cycle variation of 2.2% (Supplementary Fig. 22a). Combined with a low device-to-device

https://doi.org/10.1038/s41928-023-01056-1

variation of 5.8% (Supplementary Fig. 22b), our $MoTe_2$ synapse favourably compares with other reported three-terminal solid-state synaptic devices based on 2D materials reported in the literature (Supplementary Table 2).

As an important feature for Hebbian learning and memory, spike-timing-dependent plasticity (STDP) is vital for unsupervised learning in spiking neural networks. STDP means that the sign and magnitude of synaptic weight change are modified by the sequence and time interval Δt between the presynaptic spike V_{pre} or modulatory spike V_{mod} and postsynaptic spike V_{post} (refs. 5,18). As shown in Fig. 5c, synaptic weight increases for $\Delta t > 0$ and decreases for $\Delta t < 0$, suggesting that our $MoTe_2$ artificial heterosynapse is capable of emulating STDP through the homoeostatic function of heterosynaptic plasticity. Meanwhile, the absolute value of weight change is larger for shorter time intervals, and the dependence of weight change on interval time fits well with the asymmetric Hebbian rule with $R^2 > 0.95$ (refs. 11,42).

Similar to the function of biological heterosynaptic metaplasticity, the homosynaptic plasticity of our $MoTe_2$ artificial synapse can be regulated by the modulatory terminal. This input-non-specific modulation contributes to the reinforcement of long-term memory and provides more degree of freedom and a wider dynamic range for neuromorphic systems[34,37]. As shown in Fig. 5d, the homosynaptic LTP and LTD behaviours of the synaptic device can be effectively modulated by V_{mod} pulses. The PSC increases from ~10 pA to ~1.2 nA after 15 negative V_d pulses and drops back after one positive V_d pulse when no heterosynaptic modulation is involved. A V_{mod} of 5 V can improve the homosynaptic potentiation by increasing $V_{g,eff}$ over the channel and facilitating gas adsorption. As a result, the PSC reaches ~3.2 nA after negative V_d pulses, and the dynamic range increases by 1.6 times. Homosynaptic potentiation can also be inhibited by negative V_{mod} pulses, which suppresses p doping and reduces the dynamic range by 90%. The modulation gate voltage can be further reduced to ±1 V, leading to an increase in the dynamic range by 41% and a decrease by 60%, respectively (Supplementary Fig. 23a).

Homosynaptic STDP can also be modulated by the modulatory terminal (Fig. 5e). The synaptic weight change is negative for $\Delta t > 0$ and positive for $\Delta t < 0$ when no V_{mod} is applied. The absolute value of Δw is higher for a shorter time interval. With the modulation of a small positive (negative) gate voltage of 1 V (−1 V), gas adsorption (desorption) is facilitated, whereas gas desorption (adsorption) is mitigated, leading to an increase (decrease) in Δw for both $\Delta t > 0$ and $\Delta t < 0$. The homosynaptic STDP curves fit well with the asymmetric anti-Hebbian rule, with $R^2 > 0.99$ (ref. 42). Therefore, our $MoTe_2$ artificial synapse can emulate both asymmetric Hebbian rule (by V_g stimuli) and asymmetric anti-Hebbian rule (by V_d stimuli), which are two vital synaptic characteristics for associative learning. This ability provides more flexibility and efficiency for future neuromorphic hardware[42,45,46].

The principle of EGV-pGD provides our artificial heterosynapse with outstanding gate controllability over the homosynaptic behaviour. Improvement in gate controllability is typically realized by reducing the equivalent oxide thickness of the gate dielectric. For previously reported 2D artificial heterosynapses, modulatory voltages are no less than 2 V even if a high-κ gate dielectric with an equivalent oxide thickness of 3.1 nm is used[23,40,47–49]. However, the modulatory voltage of our $MoTe_2$ device is only 1 V using a 90 nm SiO_2 gate dielectric (Supplementary Fig. 24 shows a comparison). This low modulatory voltage leads to a reduced modulatory current (Supplementary Fig. 23b) and ultimately an ultralow modulatory power consumption of 48 fW. A comparison of the power consumption with other 2D artificial heterosynapses is shown in Fig. 5f. The energy consumption, which is 9.5 fJ, is also much lower than previously reported values (Supplementary Fig. 25)[23]. By using 35-nm-thick Al_2O_3 as the gate dielectric (Supplementary Fig. 26), the modulatory voltage, power consumption and energy consumption can be further reduced to 0.2 V, 7.3 fW and 0.73 fJ, respectively (Fig. 5f and Supplementary Figs. 24 and 25).

Based on the rich functions of the reconfigurable $MoTe_2$ device as discussed above, the reconfiguration ability of our device is demonstrated by consecutively switching four representative functions/states (Extended Data Fig. 1a). Specifically, the $MoTe_2$ device is reconfigured among the functions of the n–p diode, graded n-doped state, uniformly p-doped state and homoeostatic function of heterosynaptic plasticity for 100 times. As shown in Extended Data Fig. 1b, the rectification ratio of the diode, the on- and off-state currents of the memory function and the dynamic range of the homoeostatic function of heterosynaptic plasticity remain fairly stable and reproducible in cycles of reconfiguration. This experiment suggests that multiple functions can be achieved and reconfigured in the single $MoTe_2$ device, which can be potentially used to effectively reduce the chip area or number of devices. The device also exhibits stable performance under variable environmental conditions. As shown in Extended Data Fig. 2 and Supplementary Fig. 27, after the device is reconfigured into different functions, the rectification ratios of n–p diode, on/off ratios of memory function and dynamic ranges of heterosynaptic plasticity are almost identical under the common relative humidity ranging from 10% to 70% and oxygen concentrations from 10% to 40%. These results suggest that our reconfigurable device is fairly adaptable and invariable under variable environments. Moreover, our device also exhibits channel-thickness-independent performance of diodes and memories when the $MoTe_2$ thicknesses ranges from 2 to 11 nm, because in this thickness range, the physical adsorption sites on $MoTe_2$ are very abundant and the surface doping is not screened from the bottom layers (Supplementary Note 9).

Regarding integration-level applications in the future, the reconfigurable $MoTe_2$ device can be compatible with mature integrated circuits by using an appropriate packaging technology like that used for microelectromechanical systems (Supplementary Note 10). The rich functions of our device, including the processing power for both digital and analogue signals, can be integrated within a single advanced mixed-signal system (Supplementary Note 11). Furthermore, to demonstrate the potential of our device working with shorter channels, we fabricated a device with a 400-nm-long channel and 35-nm-thick Al_2O_3 as the gate dielectric. The device exhibits excellent current-rectifying behaviours as polarity-switchable diodes, high on/off ratio as memory and ultralow modulatory voltage and power consumption as an artificial heterosynapse, effectively demonstrating the downscaling potential of our reconfigurable devices (Supplementary Note 12).

Conclusions

We have reported the EGV-pGD method, which is collectively controlled by the gate, drain and source terminals and based on the adsorption/desorption of oxygen and water molecules. This doping method allows a single-gate $MoTe_2$ device to exhibit a variety of reconfigurable functions, including polarity-switchable diodes, memory, homosynaptic plasticity, heterosynaptic plasticity and in-memory logic (Supplementary Table 3 lists a summary of the input reconfiguration voltages for each function). The reconfigurability of our device favourably compares with previously reported 2D reconfigurable devices (Supplementary Table 1) and shows high robustness during repeated reconfigurations and under various atmospheres.

The polarity-switchable diodes show rectification ratios of 1.4×10^4 in the n–p state and 1.1×10^3 in the p–n state with photoelectric detection capability. The memory exhibits a retention time of over 36 h, endurance of 500 cycles and multilevel storage ability. The $MoTe_2$ device can emulate a biological heterosynapse with multiple plasticities. The synaptic weight can be adjusted by either homosynaptic or heterosynaptic stimuli, whereas the homosynaptic plasticity itself is modulated by heterosynaptic stimuli with an ultralow power consumption. Furthermore, in-memory NOR and AND logic gates are created. We systematically explored the correlation among drain, source and gate voltages, providing a doping method for 2D reconfigurable devices with both low structure complexity and multiple functions. The EGV-pGD strategy could be used to design reconfigurable devices and could be applied to other gate-induced doping effects beyond gas molecule adsorption/desorption, such as charge trapping and ferroelectric polarization.

Methods

Fabrication of reconfigurable $MoTe_2$ devices

$MoTe_2$ flakes were mechanically exfoliated from a commercial 2H-$MoTe_2$ bulk (2D Semiconductors) onto Si substrates with SiO_2 (thermal oxide, 90 nm thick) or Al_2O_3 (atomic layer deposition, 35 nm thick) as the back-gate dielectric. The drain and source electrodes of Ti (5 nm thick)/Au (60 nm thick) were defined onto the $MoTe_2$ flakes by standard electron-beam lithography, followed by electron-beam evaporation in a vacuum ($<5 \times 10^{-4}$ Pa) and a lift-off process in acetone. The as-fabricated devices were annealed in low-pressure-mixed 90% Ar/10% H_2 for 30 min at 140 °C to improve the electrical contacts.

Reconfiguration and electrical measurements

Reconfiguration processes and measurements of electrical characteristics were performed using a semiconductor parameter analyser (Agilent B1500A) in an electrical stage (Zhengzhou Ketan KT-Z165M4RT or Linkam T96-S). All the configuration processes and electrical tests were conducted in ambient air with a humidity of 25–45%, unless noted otherwise. Supplementary Table 3 summarizes the input reconfiguration voltages for each function. For the retention test of the $MoTe_2$ memory, the electrical stage was immediately vented after the configuration process was finished. The pressure reached 1×10^{-2} Pa in less than 4 min and stabilized at ~8×10^{-4} Pa. The optoelectrical response of the polarity-switchable diodes was measured at different power densities under a continuous white-light-emitting diode.

Characterizations

Optical images were captured by an optical microscope (Olympus BX51M). The Raman spectrum was collected by a spectrometer (Horiba iHR550) with an excitation laser of 532 nm in wavelength. Atomic force microscopy and KPFM measurements were conducted using the atomic force microscopy equipment (Bruker Multimode 8), where the samples were protected by Ar to avoid the adsorption of additional molecules or surface contamination.

Evaluation of nonlinearity

The nonlinearity value of the LTP curves is evaluated by fitting the LTP curves with the equation $G_p = G_0(1 - e^{-\upsilon p}) + G_{\min}$, where $G_0 = \frac{G_{\max} - G_{\min}}{(1 - e^{-\upsilon})}$; G_p is the electrical conductance of the LTP curves that changes with normalized pulse number p; υ is the nonlinearity value; and $G_{\max}$ and $G_{\min}$ represent the maximum and minimum values of conductance, respectively[43].

Data availability

Source data are provided with this paper. All other data that support the findings of this study are available from the corresponding author upon reasonable request.

References

1. Liu, Y. et al. Promises and prospects of two-dimensional transistors. *Nature* **591**, 43–53 (2021).
2. Monmasson, E. & Cirstea, M. N. FPGA design methodology for industrial control systems—a review. *IEEE Trans. Technol. Soc.* **54**, 1824–1842 (2007).
3. Zhao, Z., Rakheja, S. & Zhu, W. Nonvolatile reconfigurable 2D Schottky barrier transistors. *Nano Lett.* **21**, 9318–9324 (2021).
4. Pan, C. et al. Reconfigurable logic and neuromorphic circuits based on electrically tunable two-dimensional homojunctions. *Nat. Electron.* **3**, 383–390 (2020).
5. Wang, B. et al. Monolayer MoS_2 synaptic transistors for high-temperature neuromorphic applications. *Nano Lett.* **21**, 10400–10408 (2021).
6. Sangwan, V. K. et al. Multi-terminal memtransistors from polycrystalline monolayer molybdenum disulfide. *Nature* **554**, 500–504 (2018).
7. Wu, E. et al. Dynamically controllable polarity modulation of $MoTe_2$ field-effect transistors through ultraviolet light and electrostatic activation. *Sci. Adv.* **5**, eaav3430 (2019).
8. Zhang, S. et al. Lateral layered semiconductor multijunctions for novel electronic devices. *Chem. Soc. Rev.* **51**, 4000–4022 (2022).
9. Liu, C. et al. Small footprint transistor architecture for photoswitching logic and in situ memory. *Nat. Nanotechnol.* **14**, 662–667 (2019).
10. Wu, F. et al. Vertical MoS_2 transistors with sub-1-nm gate lengths. *Nature* **603**, 259–264 (2022).
11. Wang, X. et al. Grain-boundary engineering of monolayer MoS_2 for energy-efficient lateral synaptic devices. *Adv. Mater.* **33**, e2102435 (2021).
12. Zhao, B. et al. High-order superlattices by rolling up van der Waals heterostructures. *Nature* **591**, 385–390 (2021).
13. Chang, Y.-M. et al. Reversible and precisely controllable p/n-type doping of $MoTe_2$ transistors through electrothermal doping. *Adv. Mater.* **30**, e1706995 (2018).
14. Seo, S.-Y. et al. Reconfigurable photo-induced doping of two-dimensional van der Waals semiconductors using different photon energies. *Nat. Electron.* **4**, 38–44 (2021).
15. Yang, F.-S. et al. Oxidation-boosted charge trapping in ultra-sensitive van der Waals materials for artificial synaptic features. *Nat. Commun.* **11**, 2972 (2020).
16. Chen, L. et al. A van der Waals synaptic transistor based on ferroelectric $Hf_{0.5}Zr_{0.5}O_2$ and 2D tungsten disulfide. *Adv. Electron. Mater.* **6**, 2000057 (2020).
17. Wu, G. et al. $MoTe_2$ p-n homojunctions defined by ferroelectric polarization. *Adv. Mater.* **32**, e1907937 (2020).
18. Xue, F. et al. Giant ferroelectric resistance switching controlled by a modulatory terminal for low-power neuromorphic in-memory computing. *Adv. Mater.* **33**, e2008709 (2021).
19. Sun, Y. et al. Versatile logic and nonvolatile memory based on a van der Waals heterojunction. *ACS Appl. Electron. Mater.* **3**, 3079–3084 (2021).
20. Li, D. et al. Two-dimensional non-volatile programmable p-n junctions. *Nat. Nanotechnol.* **12**, 901–906 (2017).
21. Huang, W. et al. Gate-coupling-enabled robust hysteresis for nonvolatile memory and programmable rectifier in van der Waals ferroelectric heterojunctions. *Adv. Mater.* **32**, e1908040 (2020).
22. Lee, S.-J. et al. Programmable devices based on reversible solid-state doping of two-dimensional semiconductors with superionic silver iodide. *Nat. Electron.* **3**, 630–637 (2020).
23. Xiong, X. et al. Reconfigurable logic-in-memory and multilingual artificial synapses based on 2D heterostructures. *Adv. Funct. Mater.* **30**, 1909645 (2020).
24. Cheng, R. et al. High-performance, multifunctional devices based on asymmetric van der Waals heterostructures. *Nat. Electron.* **1**, 356–361 (2018).
25. Ruppert, C., Aslan, O. B. & Heinz, T. F. Optical properties and band gap of single- and few-layer $MoTe_2$ crystals. *Nano Lett.* **14**, 6231–6236 (2014).
26. Zhang, X. et al. Surface charge transfer doping of low-dimensional nanostructures toward high-performance nanodevices. *Adv. Mater.* **28**, 10409–10442 (2016).
27. Tongay, S. et al. Broad-range modulation of light emission in two-dimensional semiconductors by molecular physisorption gating. *Nano Lett.* **13**, 2831–2836 (2013).

28. Cho, K. et al. Electric stress-induced threshold voltage instability of multilayer MoS_2 field effect transistors. *ACS Nano* **7**, 7751–7758 (2013).
29. Ding, G. et al. Reconfigurable 2D WSe_2-based memtransistor for mimicking homosynaptic and heterosynaptic plasticity. *Small* **17**, e2103175 (2021).
30. Kang, M. S. & Frisbie, C. D. A pedagogical perspective on ambipolar FETs. *ChemPhysChem* **14**, 1547–1552 (2013).
31. Sze, S. M. & Ng, K. K. *Physics of Semiconductor Devices* 3rd edn (Wiley-Interscience, 2007).
32. Das, S., Dodda, A. & Das, S. A biomimetic 2D transistor for audiomorphic computing. *Nat. Commun.* **10**, 3450 (2019).
33. Li, E. et al. MXene based saturation organic vertical photoelectric transistors with low subthreshold swing. *Nat. Commun.* **13**, 2898 (2022).
34. Purves, D. (ed). *Neuroscience* 6th edn (Sinauer Associates, 2018).
35. Chistiakova, M. et al. Heterosynaptic plasticity: multiple mechanisms and multiple roles. *Neuroscientist* **20**, 483–498 (2014).
36. Chater, T. E. & Goda, Y. My neighbour hetero-deconstructing the mechanisms underlying heterosynaptic plasticity. *Curr. Opin. Neurobiol.* **67**, 106–114 (2021).
37. Fernandes, D. & Carvalho, A. L. Mechanisms of homeostatic plasticity in the excitatory synapse. *J. Neurochem.* **139**, 973–996 (2016).
38. Abraham, W. C. Metaplasticity: tuning synapses and networks for plasticity. *Nat. Rev. Neurosci.* **9**, 387 (2008).
39. Bailey, C. H. et al. Is heterosynaptic modulation essential for stabilizing Hebbian plasticity and memory? *Nat. Rev. Neurosci.* **1**, 11–20 (2000).
40. Nam, J. H. et al. Low power MoS_2/Nb_2O_5 memtransistor device with highly reliable heterosynaptic plasticity. *Adv. Funct. Mater.* **31**, 2104174 (2021).
41. Huh, W. et al. Synaptic barristor based on phase-engineered 2D heterostructures. *Adv. Mater.* **30**, 1801447 (2018).
42. John, R. A. et al. Synergistic gating of electro-iono-photoactive 2D chalcogenide neuristors: coexistence of Hebbian and homeostatic synaptic metaplasticity. *Adv. Mater.* **30**, e1800220 (2018).
43. Seo, S. et al. An optogenetics-inspired flexible van der Waals optoelectronic synapse and its application to a convolutional neural network. *Adv. Mater.* **33**, e2102980 (2021).
44. Lim, S. et al. Adaptive learning rule for hardware-based deep neural networks using electronic synapse devices. *Neural Comput. Appl.* **31**, 8101–8116 (2019).
45. Hussain, S., Liu, S.-C. & Basu, A. Hardware-amenable structural learning for spike-based pattern classification using a simple model of active dendrites. *Neural Comput.* **27**, 845–897 (2015).
46. D'Souza, P., Liu, S.-C. & Hahnloser, R. H. R. Perceptron learning rule derived from spike-frequency adaptation and spike-time-dependent plasticity. *Proc. Natl Acad. Sci. USA* **107**, 4722–4727 (2010).
47. Wang, L. et al. Artificial synapses based on multiterminal memtransistors for neuromorphic application. *Adv. Funct. Mater.* **29**, 1901106 (2019).
48. He, C. et al. Artificial synapse based on van der Waals heterostructures with tunable synaptic functions for neuromorphic computing. *ACS Appl. Mater. Interfaces* **12**, 11945–11954 (2020).
49. Zhang, P. et al. Transition from trap-mediated to band-like transport in polycrystalline monolayer molybdenum disulfide memtransistors. *Appl. Phys. Lett.* **117**, 223101 (2020).
50. Tian, H. et al. Emulating bilingual synaptic response using a junction-based artificial synaptic device. *ACS Nano* **11**, 7156–7163 (2017).
51. Lee, H.-S. et al. Dual-gated MoS_2 memtransistor crossbar array. *Adv. Funct. Mater.* **30**, 2003683 (2020).
52. Jadwiszczak, J. et al. MoS_2 memtransistors fabricated by localized helium ion beam irradiation. *ACS Nano* **13**, 14262–14273 (2019).
53. Nguyen, D. A. et al. Electrically and optically controllable p-n junction memtransistor based on an Al_2O_3 encapsulated 2D Te/ReS_2 van der Waals heterostructure. *Small Methods* **5**, e2101303 (2021).

Acknowledgements

We thank Z. Wang, H. Tian and J. Tang for the helpful discussions. This work was financially supported by the Basic Science Center Project of NSFC under grant no. 52388201 (K.L.); the National Key R&D Program of China under grant nos. 2022YFA1203400 (K.L.), 2018YFA0208401 (K.L.) and 2021YFA1200800 (C.W.); and the National Natural Science Foundation of China under grant nos. 51972193 (K.L.), 61925402 (P.Z.), 12241404 (C.S.), 52225106 (C.S.), 62004114 (C.W.) and 62174098 (C.W.).

Author contributions

K.L. and R.P. conceived the idea and designed the experiments. R.P., Y.W., B.W. and T.P. fabricated the devices. R.P. performed the KPFM measurements. R.P., J.G. and B.Z. carried out the electrical measurements for different device functions. R.P., K.L., R.S., C.S., Z.F., C.W., P.Z. and S.F. analysed the data. R.P. and K.L. drafted the paper. All the authors contributed to the discussions and the final version of the paper.

Competing interests

The authors declare no competing interests.

Additional information

Extended data is available for this paper at https://doi.org/10.1038/s41928-023-01056-1.

Supplementary information The online version contains supplementary material available at https://doi.org/10.1038/s41928-023-01056-1.

Correspondence and requests for materials should be addressed to Kai Liu.

Peer review information *Nature Electronics* thanks Ye Zhou, Enxiu Wu and the other, anonymous, reviewer(s) for their contribution to the peer review of this work.

Reprints and permissions information is available at www.nature.com/reprints.

https://doi.org/10.1038/s41928-023-01056-1

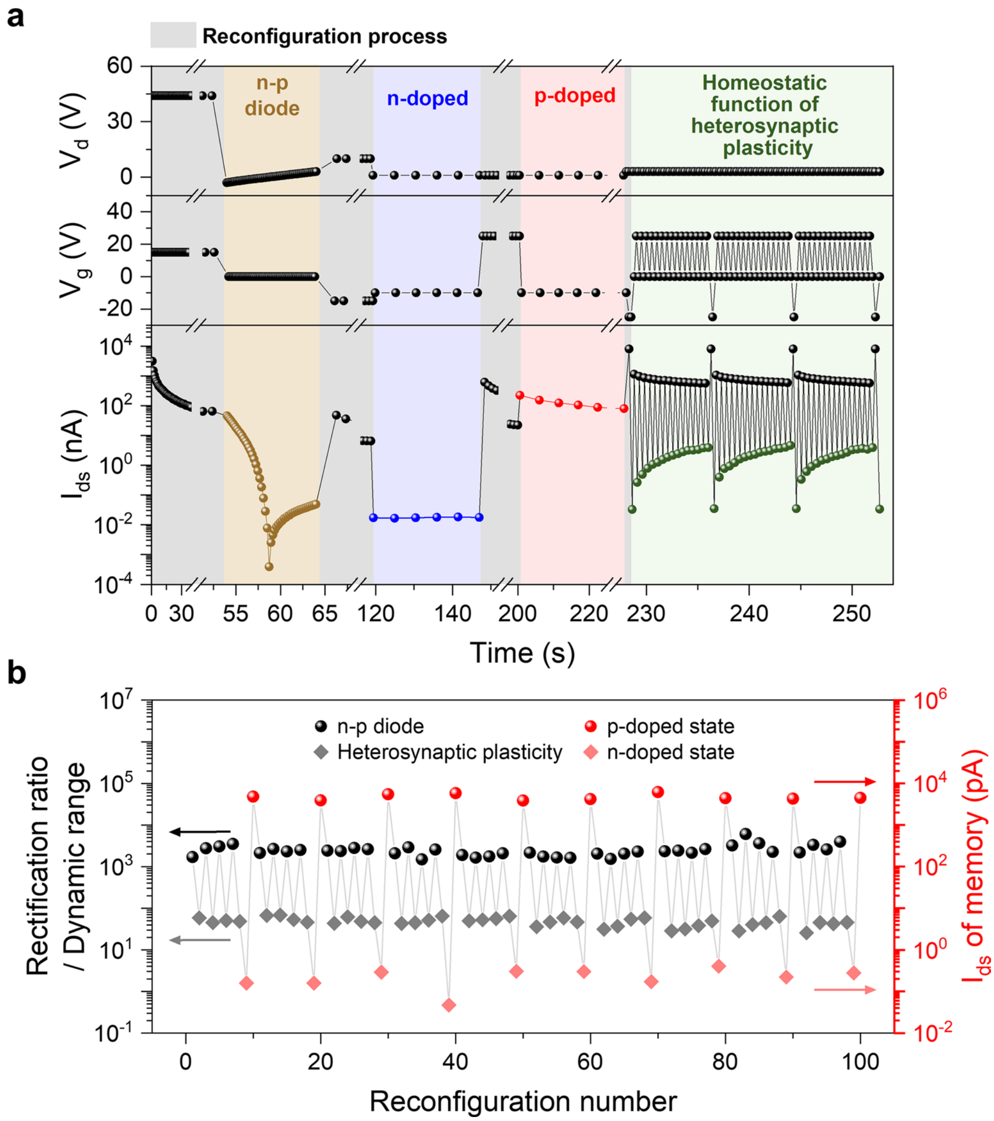

Extended Data Fig. 1 | Consecutive reconfiguration of our MoTe$_2$ devices. **a**, Consecutive switches of four functions among n-p diode, n-doped state, p-doped state, and homeostatic function of heterosynaptic plasticity. The coloured background regions represent the electrical characterization process of each function and the grey regions mark the reconfiguration processes. V_d/V_g sets of 44 V/15 V, 10 V/−15 V, and 1 V/25 V are applied for the reconfiguration process of n-p diode, n-doped state, and p-doped state, respectively. Positive V_g pulses of 25 V, 0.1 s and negative V_g pulses of −25 V, 0.15 s are applied for the emulation of homeostatic function of heterosynaptic plasticity. **b**, Rectification ratio of n-p diode, dynamic range of homeostatic function of heterosynaptic plasticity, and channel currents of n-doped state and p-doped state of memory in repeated function switches.

https://doi.org/10.1038/s41928-023-01056-1

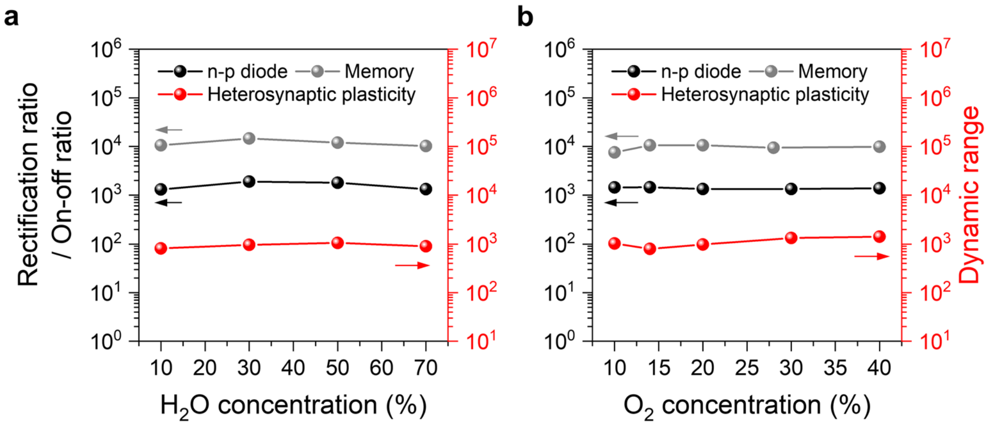

Extended Data Fig. 2 | Performance of reconfigurable $MoTe_2$ device under variable environmental conditions. **a**, Performance of the device under variable environmental relative humidity. The oxygen content was kept at 20%. **b**, Performance of the device under variable oxygen concentration. The relative humidity was kept at 10%. All of the measurements were carried out at room temperature. All data are extracted from the corresponding raw data in Supplementary Fig. 27. Rectification ratio is extracted for n-p diode function, on/off ratio for memory, and dynamic range for homeostatic function of heterosynaptic plasticity.